Resolution and Denoising in Near-Field Imaging

Grégoire Derveaux†, George Papanicolaou‡ and Chrysoula Tsogka¶

† INRIA, BP 105, 78150 Le Chesnay Cedex, France
‡ Department of Mathematics, Stanford University, Stanford, CA 94301
¶ Department of Mathematics, University of Chicago, Chicago, IL 60637

E-mail: gregoire.derveaux@inria.fr, papanico@math.stanford.edu and tsogka@math.uchicago.edu

Submitted to: *Inverse Problems*

Abstract.

We consider the inverse problem of reconstructing surface displacements from noisy acoustic measurements collected at a distance from the surface that is comparable to the wavelength. As the detectors move closer to the surface and information from evanescent waves is recorded, the resolution of the image improves up to a level that is limited by the signal to noise ratio (SNR). We review this basic trade-off in near-field imaging with narroband signals and then extend it to broadband signals. We find that the resolution in broadband near-field imaging is enhanced because the SNR effectively increases with increasing bandwidth. We present the results of numerical simulations to illustrate this enhancement of the resolution.

PACS numbers: 43.60.Gk, 43.60.Cg, 43.60.Rw, 43.60 Tj

1. Introduction

We consider the problem of near-field imaging of surface displacements with noisy measurements made with a planar array of sensors. We assume that a known incident field impinges on the surface to be imaged and the scattered field is measured very close to it so that exponentially small, evanescent components of the waves are significant and can be measured. The resulting resolution enhancement is, however, limited by the amount of the noise in the data, the signal to noise ratio (SNR).

This problem is similar to near-field acoustical holography (NAH), a technique that was initially introduced in [21, 22] for imaging sources in air using planar arrays. Since then the method has been generalized to imaging underwater sources [18] and to more general array geometries [19, 7]. The basic difference between NAH and classic holography is that in NAH evanescent components of the waves are used in the reconstructions. To be able to record these exponentially small evanescent components of the waves the measurements have to be made very close to the surface. When this is possible and such evanescent waves are used in the inversion, the imaging resolution can be much better than the wavelength of the incident field. According to the Rayleigh criterion [8, 17], when only far field measurements are used then the image resolution is proportional to the wavelength. Thus, by using near-field measurements, it is possible to improve considerably the Rayleigh resolution [21, 2, 3].

The main issue in near-field imaging is noise amplification. It arises from the inversion of evanescent waves, which means that the noisy measurements are multiplied by exponentially increasing functions. Thus, there is an important trade-off in near-field imaging between resolution and the signal to noise ratio (SNR) of the data. A careful SNR analysis of the near-field data measurements is needed, along with a regularization of the inversion. In [3, 21] this analysis has been carried out for monochromatic incident waves and a cut-off regularization method is used. Several other regularization methods applied to NAH are considered in [23]. We do not address the issue of regularization methods here, and consider only a cut-off based regularization. We note that NAH is a monochromatic inversion method. A generalization to broadband excitation was proposed in [20] where, however, the SNR issue was not considered.

In this paper we consider the reduction of noise effects by using a broadband incident wave. Regularization is still needed for the inversion and we consider two cut-off methods here that generalize the narrowband cut-off method used in [3]. The use of broadband signals for improving image resolution by effectively reducing the noise in the data by averaging over frequencies has not been considered previously, to the best of our knowledge. We consider here an additive Gaussian white noise model, both in time and space, and we show that near-field resolution in broadband regimes is considerably better than in narrowband regimes. We illustrate this effect with several results of numerical simulations.

Although, there has been a lot of interest in near-field imaging motivated by different applications, like for example in near-field optics [11, 12, 1, 10], or detection of buried objects with a radar [16], there seems to be no adequate resolution theory that accounts for: (a) full scattering and not only single scattering (Born approximation), (b) multiple scattering from clutter near the object to be imaged and (c) noise in the measurements. When only single scattering and measurement noise are considered, in the narrowband regime, a near-field resolution theory can be developed [2, 3]. We review it briefly here before generalizing it to the broadband regime. In the far-field

measurement noise is less important, since evanescent modes are absent, but clutter is important. Some recent results in far field array imaging in clutter are presented in [4, 5, 6].

The paper is organized as follows. In section §2 we give the analytical formulation of the problem. The narrowband inversion method is reviewed in section §3 for both far-field and near-field measurements, and the results of numerical simulations are presented. In section §4 we present the analysis of broadband inversion with two cut-off regularization methods. The improvement in resolution compared to the narrowband case is illustrated with several numerical results. We end with a brief summary and conclusions in section §5.

2. Formulation of the problem

2.1. The surface scattering model

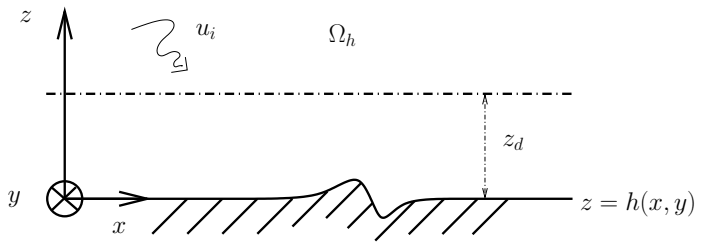

Figure 1. The surface displacement is described by a time independent function $z = h(x, y)$. An incident field u_i is impinging on this surface which is assumed to be a perfect reflector. Measurements of the scattered field are made at distance z_d from the surface.

We want to image small surface displacements of a plane surface with measurements of reflected waves at distance z_d from it (see figure 1). The surface displacement is described by the function $h(x, y)$ and the domain of interest is the half space Ω_h defined by $\Omega_h = \{(x, y, z) \in \mathbb{R}^3 \ / \ z > h(x, y)\}$. In the following, we use the notation $\boldsymbol{r} = (x, y, z)$, $\boldsymbol{\rho} = (x, y)$ and $r = |\boldsymbol{r}| = \sqrt{x^2 + y^2 + z^2}$.

We consider an incident wave u_i impinging on the domain Ω_h. We want to characterize the scattered field u_s produced by reflection from the boundary of Ω_h. In the frequency domain, the scattered field u_s is the solution of the Helmholtz equation with Dirichlet boundary condition on $z = h(\boldsymbol{\rho})$:

$$\begin{cases} (a) \quad \Delta u_s + k^2 u_s = 0, & \text{in } \Omega_h, \\ (b) \quad u_s(\boldsymbol{\rho}, h(\boldsymbol{\rho})) = -u_i(\boldsymbol{\rho}, h(\boldsymbol{\rho})), & \forall \boldsymbol{\rho} \in \mathbb{R}^2, \\ (c) \quad \lim_{r \to \infty} (\partial_r u_s - iku_s) = 0. \end{cases} \tag{1}$$

Here, $k = \omega/c$ is the wave number, ω is the angular frequency and c is the speed of light. The associated wavelength is $\lambda = 2\pi/k$. Equation (1c) is the usual Sommerfeld radiation condition.

Assuming that the displacement is sufficiently small, i.e., assuming $\max_{\boldsymbol{\rho}} |h(\boldsymbol{\rho})| \ll \lambda$, the boundary condition (1b) can be approximated by:

$$u_s(\boldsymbol{\rho}, 0) + h(\boldsymbol{\rho}) \partial_z u_s(\boldsymbol{\rho}, 0) \approx -u_i(\boldsymbol{\rho}, 0) - h(\boldsymbol{\rho}) \partial_z u_i(\boldsymbol{\rho}, 0), \quad \forall \boldsymbol{\rho} \in \mathbb{R}^2. \tag{2}$$

This is the Born approximation, which consists in neglecting multiple reflections and so the second term of the left hand side is dropped. Introducing the scattered field u_0 produced by the flat surface, the measured field $u = u_s - u_0$ satisfies the equation

$$\begin{cases} (a) \quad \Delta u + k^2 u = 0, & \text{in } \Omega_0 = \{(x, y, z),\ z > 0\}, \\ (b) \quad u(\boldsymbol{\rho}, 0) = -h(\boldsymbol{\rho})\partial_z u_i(\boldsymbol{\rho}, 0), & \forall \boldsymbol{\rho} \in \mathbb{R}^2, \\ (c) \quad \lim_{r\to\infty} (\partial_r u - iku) = 0. \end{cases} \tag{3}$$

In the following we write $f(\boldsymbol{\rho}) = -h(\boldsymbol{\rho})\partial_z u_i(\boldsymbol{\rho}, 0)$ and we call it the surface displacement.

We assume that the scattered field amplitude is measured in all the plane $z = z_d$ and is corrupted by additive noise, so that the data to invert have the form

$$g_{z_d}(\boldsymbol{\rho}) = u(\boldsymbol{\rho}, z_d) + n(\boldsymbol{\rho}). \tag{4}$$

The noise $n(\boldsymbol{\rho})$ is a stationary process with mean zero and covariance $R_{nn}(\boldsymbol{\rho})$. The inverse problem that we want to solve is the following: *given the measured field in the plane $z = z_d$, that is given $g_{z_d}(\boldsymbol{\rho})$, we want to recover the surface displacement $f(\boldsymbol{\rho})$.*

2.2. Spectral representation

The solution u of (3) can be expressed as a superposition of plane waves [14] by using the Fourier Transform in the transverse coordinates $\boldsymbol{\rho} = (x, y)$

$$\begin{cases} \partial_z^2 \hat{u}(\boldsymbol{\kappa}, z) + (k^2 - |\boldsymbol{\kappa}|^2)\hat{u}(\boldsymbol{\kappa}, z) = 0, & \forall \boldsymbol{\kappa} \in \mathbb{R}^2 \text{ and } \forall z > 0, \\ \hat{u}(\boldsymbol{\kappa}, 0) = \hat{f}(\boldsymbol{\kappa}), & \forall \boldsymbol{\kappa} in \mathbb{R}^2, \\ \text{Radiation condition at } \infty. \end{cases} \tag{5}$$

This gives

$$u(\boldsymbol{\rho}, z_d) = \frac{1}{(2\pi)^2} \int_{\boldsymbol{\kappa}} \hat{f}(\boldsymbol{\kappa}) e^{i(\boldsymbol{\rho}.\boldsymbol{\kappa} + z_d k_z(\boldsymbol{\kappa}))} d\boldsymbol{\kappa}, \tag{6}$$

where

$$k_z(\boldsymbol{\kappa}) = \sqrt{k^2 - |\boldsymbol{\kappa}|^2} \tag{7}$$

and $|\boldsymbol{\kappa}|^2 = \kappa_x^2 + \kappa_y^2$, with the square root of negative numbers chosen to have positive imaginary part. Thus, at a given height for the measurements z_d, the Fourier transform of the scattered field $\hat{u}(\boldsymbol{\kappa}, z_d)$ is

$$\hat{u}(\boldsymbol{\kappa}, z_d) = \hat{S}_{z_d}(\boldsymbol{\kappa})\hat{f}(\boldsymbol{\kappa}). \tag{8}$$

The multiplier $\hat{S}_{z_d}(\boldsymbol{\kappa})$ is the transfer function of the imaging system and is given by

$$\hat{S}_{z_d}(\boldsymbol{\kappa}) = e^{iz_d k_z(\boldsymbol{\kappa})}. \tag{9}$$

Plane waves with $|\boldsymbol{\kappa}| \leq k$ are propagating in the z direction without any decay. They carry information about features of the surface displacement f whose size is of the order of the wavelength $\lambda = 2\pi/k$. On the other hand plane waves corresponding to $|\boldsymbol{\kappa}| > k$ are evanescent in the z direction and they decay as $e^{-z_d\sqrt{|\boldsymbol{\kappa}|^2 - k^2}}$. These waves carry information about spatial features of f which are smaller than the wave length. At higher observation distances z_d the information in evanescent modes will get lost in noisy measurements. Therefore two regions of observation are distinguished:

- The far-field region, corresponding to observation distances larger than the wavelength, $z_d >> \lambda$. In this case the evanescent waves can be neglected.
- The near-field region, corresponding to observation distances smaller than the wavelength, $z_d < \lambda$. In this case the evanescent waves can be used.

3. Inversion with far-field data versus inversion with near-field data

In the Fourier domain, as in (8), the inverse problem to be solved has the form

$$\hat{g}(\boldsymbol{\kappa}) = \hat{S}_{z_d}(\boldsymbol{\kappa})\hat{f}(\boldsymbol{\kappa}) + \hat{n}(\boldsymbol{\kappa}). \tag{10}$$

The Fourier transform of the noise process, $\hat{n}(\boldsymbol{\kappa})$, is a zero mean process with orthogonal increments

$$E\{\hat{n}(\boldsymbol{\kappa})\overline{\hat{n}(\boldsymbol{\kappa}')}\} = \delta(\boldsymbol{\kappa} - \boldsymbol{\kappa}')\hat{R}_{nn}(\boldsymbol{\kappa}), \tag{11}$$

where $\hat{R}_{nn}(\boldsymbol{\kappa})$ is the power spectral density, that is, the Fourier transform of the covariance $R_{nn}(\boldsymbol{\rho})$.

We will now consider how the unknown surface displacement f, or equivalently its Fourier Transform $\hat{f}$, can be recovered from far-field or near-field data. The results presented briefly in this section are a summary of the inverse diffraction problem from plane to plane, described in a paper of Bertero *et al.* [2] and we refer to this paper for further details.

3.1. Far-field inversion

Only information carried by the propagating waves is used for the reconstruction of the unknown $f(\boldsymbol{\rho})$. The evanescent waves are thus neglected in (9). In that case $|\hat{S}_{z_d}(\boldsymbol{\kappa})| \leq 1$ so (10) can be solved for $f(\boldsymbol{\rho})$ since there is no noise amplification. The *far field* estimate for $\hat{f}(\boldsymbol{\kappa})$ is thus

$$\hat{f}^{FF}(\boldsymbol{\kappa}) = e^{-iak_z(\boldsymbol{\kappa})}\hat{g}(\boldsymbol{\kappa}), \quad \text{for } |\boldsymbol{\kappa}| \leq k \text{and zero otherwise.} \tag{12}$$

If we introduce the inverse of the transfer function $\hat{S}_{z_d}$,

$$\hat{S}^{FF-}_{z_d}(\boldsymbol{\kappa}) = \begin{cases} e^{-iak_z(\boldsymbol{\kappa})} & \text{for } |\boldsymbol{\kappa}| \leq k, \\ 0 & \text{else,} \end{cases} \tag{13}$$

we can write the far field estimate in the form

$$\hat{f}^{FF}(\boldsymbol{\kappa}) = \mathbf{1}_k(\boldsymbol{\kappa})\hat{f}(\boldsymbol{\kappa}) + \hat{S}^{FF-}_{z_d}(\boldsymbol{\kappa})\hat{n}(\boldsymbol{\kappa}), \quad \forall \boldsymbol{\kappa} \in \mathbb{R}^2. \tag{14}$$

Here $\mathbf{1}_k$ denotes the characteristic function of the spatial frequency band $\mathcal{B}_k = \{\boldsymbol{\kappa}, |\boldsymbol{\kappa}| \leq k\}$.

The first term of this expression is a low pass filtered function of $\hat{f}$. In the space domain it is a convolution with the *point spread function* kernel

$$\mathcal{K}^{FF}(\boldsymbol{\rho}) = kJ_1(k|\boldsymbol{\rho}|)/(2\pi|\boldsymbol{\rho}|),$$

where J_1 is the first order Bessel function of the first kind. The resolution limit from this term is the famous Rayleigh limit [8, 17, 2]: only spatial features of f that are greater than R_{FF} can be distinguished where R_{FF}, the distance of the central peak of $\mathcal{K}^{FF}$to its first zero, is given by

$$R_{FF} = 1.22\frac{\pi}{k} = 1.22\frac{\lambda}{2}. \tag{15}$$

The second term of (14) is the noise after low pass filtering. Since $|\hat{S}_{z_d}^{FF-}(\boldsymbol{\kappa})| \leq 1, \forall \boldsymbol{\kappa} \in \mathbb{R}^2$, this noise term is not amplified by the inversion. Thus, as far as corruption by noise of the reconstructed surface displacement is concerned, the estimate provided by (14) is stable in the sense that the noise is not amplified. Also, since the propagating waves are traveling without decay, the images obtained from far-field data do not depend on the distance z_d .

3.2. Near-field inversion

Information carried by the evanescent waves is now used to reconstruct the surface displacement. This means that we solve equation (10) without neglecting the evanescent modes which makes the problem ill posed. Following [2, 21] we regularize it by truncation. This consists in taking into account only the evanescent waves whose amplitude is greater than the noise level. Note that other regularization techniques can be used [9, 23]. We do not address the question of the regularization method in this paper and present only the cut-off regularization. We obtain the following estimate

$$\hat{f}^{NF}(\boldsymbol{\kappa}) = \hat{S}_{z_d}^{NF-}(\boldsymbol{\kappa})\hat{g}(\boldsymbol{\kappa}), \tag{16}$$

where

$$\hat{S}_{z_d}^{NF-}(\boldsymbol{\kappa}) = \begin{cases} e^{-iz_d k_z(\boldsymbol{\kappa})} & \text{for } |\boldsymbol{\kappa}| \leq k_{NF}, \\ 0 & \text{for } |\boldsymbol{\kappa}| > k_{NF}. \end{cases} \tag{17}$$

Here the cut-off wavenumber $k_{NF} > k$ is defined by

$$k_{NF} = \max\left\{ |\boldsymbol{\kappa}|, \ \left|\hat{S}_{z_d}(\boldsymbol{\kappa})\right| \geq \frac{1}{\mathrm{SNR}} \right\}, \tag{18}$$

and SNR is an estimate of the signal-to-noise ratio. A determination of this cut-off from a formulation of near-field imaging as a deblurring problem [9, 15] is given in the next subsection. Using (10) in (16) we can write the near-field estimate of the surface displacement in the form

$$\hat{f}^{NF}(\boldsymbol{\kappa}) = \mathbf{1}_{k_{NF}}(\boldsymbol{\kappa})\hat{f}(\boldsymbol{\kappa}) + \hat{S}_{z_d}^{NF-}(\boldsymbol{\kappa})\hat{n}(\boldsymbol{\kappa}), \quad \forall \boldsymbol{\kappa} \in \mathbb{R}^2. \tag{19}$$

The first term has clearly better resolution compared to (14) since $k_{NF} > k$, with SNR > 1. A calculation similar to the one used for the Rayleigh resolution criterion shows that features of f on scales greater than R_{NF} can be recovered, where

$$R_{NF} = \frac{1.22\pi}{k_{NF}} = \frac{R_{FF}}{\left[1 + \frac{1}{4\pi^2}\left(\frac{\lambda}{z_d}\right)^2 \log^2 \mathrm{SNR}\right]^{\frac{1}{2}}} < R_{FF}. \tag{20}$$

This resolution limit is a decreasing function of the distance of observation z_d and an increasing function of the signal-to-noise ratio SNR. Table 1 gives some values of the ratio R_{FF}/R_{NF} for several values of distance of observation and SNR.

The improvement in resolution in near-field inversion, compared to the far-field one, can be very substantial if measurements are made very close to the surface. For example, the resolution is increased by a factor 73 when $z_d = \lambda/100$ and SNR $= 40$ dB. Moreover, the rate of improvement increases as measurements are made closer to the surface. This is shown in figure 2 where the resolution limit is plotted as a function of the distance of observation, relative to the wavelength λ and for a given signal to noise ratio. If measurements are made at a distance greater than the wavelength then there is no significant resolution improvement.

	Distance of observation z_d/λ					
SNR	1/100	1/10	1/5	1/2	1	2
40 dB	73.300	7.397	3.798	1.774	1.239	1.065
20 dB	36.660	3.798	2.087	1.239	1.065	1.016
12 dB	22.086	2.422	1.489	1.093	1.024	1.006

Table 1. Improvement of the resolution in near-field imaging: values of R_{FF}/R_{NF} for different values of noise and observation distance.

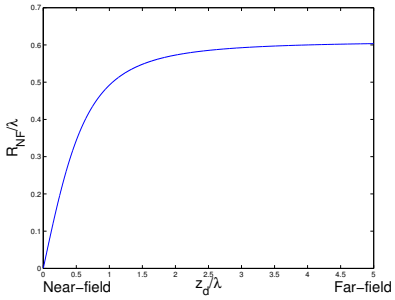

Figure 2. Dimensionless resolution R_{NF}/λ versus dimensionless distance of observation z_d/λ, relative to the wavelength λ, for SNR $= 40$ dB

Table 1 shows also the important influence of SNR on the resolution improvement. The ratio R_{FF}/R_{NF} decreases from 73 to 36 at observation distance $z_d = \lambda/100$ when the SNR decreases from 40dB to 20dB. This is a consequence of the corruption of evanescent waves by noise.

3.3. Deblurring formulation of near-field imaging

We can give a more precise algorithm for estimating the cut-off wavenumber k_{NF} of (18) and of (20) by reformulating near-field imaging as a deblurring problem [9, 15].

The difference between the estimate $\hat{f}^{NF}(\boldsymbol{\kappa})$ of (19) and the true surface displacement $\hat{f}(\boldsymbol{\kappa})$ is

$$\hat{e}^{NF}(\boldsymbol{\kappa}) = \hat{f}^{NF}(\boldsymbol{\kappa}) - \hat{f}(\boldsymbol{\kappa}) = (1 - \mathbf{1}_{k_{NF}}(\boldsymbol{\kappa}))\hat{f}(\boldsymbol{\kappa}) + \hat{S}^{NF^-}_{z_d}(\boldsymbol{\kappa})\hat{n}(\boldsymbol{\kappa}).$$

If Δ is any interval of horizontal wavenumbers $\boldsymbol{\kappa}$ then

$$\frac{1}{\Delta}E\{(\int_{\Delta}(\hat{e}^{NF}(\boldsymbol{\kappa}))^2 d\boldsymbol{\kappa}\} = \begin{cases} \frac{1}{\Delta}\int_{\Delta}(\hat{S}^{NF}_{z_d}(\boldsymbol{\kappa}))^{-2}\hat{R}_{nn}(\boldsymbol{\kappa})d\boldsymbol{\kappa}, & \Delta \subset \{|\boldsymbol{\kappa}| \leq k_{NF}\}, \\ \frac{1}{\Delta}\int_{\Delta}(\hat{f}(\boldsymbol{\kappa}))^2 d\boldsymbol{\kappa}, & \Delta \subset \{|\boldsymbol{\kappa}| > k_{NF}\}. \end{cases} \quad (21)$$

Let

$$P^2 = \max_{\boldsymbol{\kappa}} |\hat{f}(\boldsymbol{\kappa})|^2,$$

be the signal power and

$$N^2 = \max_{\boldsymbol{\kappa}} \hat{R}_{nn}(\boldsymbol{\kappa}),$$

be the noise power, with the signal to noise ratio defined by

$$SNR = \frac{P}{N}.$$

Then

$$\lim_{\Delta\to 0}\frac{1}{\Delta}E\{(\int_{\Delta}(\hat{e}^{NF}(\boldsymbol{\kappa}))^2 d\boldsymbol{\kappa}\}\leq\begin{cases}(\hat{S}^{NF}_{z_d}(\boldsymbol{\kappa}))^{-2}N^2, & |\boldsymbol{\kappa}|\leq k_{NF}\\ P^2, & |\boldsymbol{\kappa}|>k_{NF}\end{cases}\tag{22}$$

and if we now choose k_{NF} so that $(\hat{S}^{NF}_{z_d}(k_{NF}))^{-2}N^2=P^2$, we obtain

$$\max_{\boldsymbol{\kappa}}\lim_{\Delta\to 0}\frac{1}{\Delta}E\{(\int_{\Delta}(\hat{e}^{NF}(\boldsymbol{\kappa}))^2 d\boldsymbol{\kappa}\}\leq P^2.$$

The near-field cut-off wavenumber is thus given by

$$\left(\frac{k_{NF}}{k}\right)^2=1+\left(\frac{\log SNR}{kz_d}\right)^2,$$

which is the same as the cut-off wavenumber in (20).

The resulting cut-off wavenumber obtained with this calculation depends mainly on: (i) the form of the regularization used, *i.e.*, in our case we seek the surface displacement as a function that has a compactly supported Fourier transform. (ii) the way the estimation error is minimized, that is, the norm used in the minimization and the criterion employed for selecting k_{NF}.

3.4. Numerical examples

In the following numerical experiments, we give some examples of reconstructions obtained with far-field and near-field data measurements for two incident fields: a single monochromatic plane wave and a beam of monochromatic plane waves.

3.4.1. Description of the numerical experiments The following experiments are realized at central frequency $f_0=5$ GHz associated to the central wavelength $\lambda_0=6$ cm. All dimensions of the problem are given with respect to the central wavelength. The object to be recovered consists in 2 disks of diameter $\lambda_0/2$ with centers separated by $3\lambda_0/4$, so that the distance between the two objects is $\lambda_0/4$. One of the disks is 1 μm high and the other is 2 μm high (see figure 3).

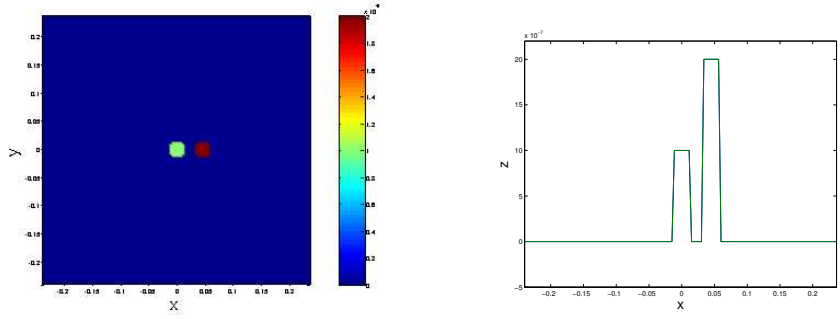

2D linear scale *1D section in the plane $y=0$*

Figure 3. Original shape: two disks of diameter $\lambda_0/2$ and separated by a distance of $\lambda_0/4$. One is 1 μm high and the other is 2 μm high.

The measurements are realized at distance z_d above the plane $z=0$, on a two dimensional array composed by a 128×128 points separated by the space step

$\Delta x = \lambda_0/16$. The propagated field $u(\boldsymbol{\rho}, z_d)$ is computed by FFT using (8) and the measurements are corrupted by additive white Gaussian noise with standard deviation σ. The value of σ is defined as a given percentage s of the L^2 norm of the propagated signal so that $\sigma = s \parallel (|u(\boldsymbol{\rho}, z_d)|) \parallel_{L^2}$. The corresponding value of the signal to noise ratio used in formula (18) is thus SNR $= s$ or in decibels, SNR $= 20 \log_{10} s$ dB.

We first consider a case with high signal-to-noise ratio, SNR= 40dB. For each incident field, the image is reconstructed using far-field data measured at $z_d = 5\lambda_0$ and using near-field data measured at the following distances: $z_d = \lambda_0/10$, $z_d = \lambda_0/2$ and $z_d = 2\lambda_0$. In addition, in order to analyze the effect of noise, we also consider a case with lower signal-to-noise ratio, SNR= 12dB. For that latter case, the image is reconstructed using far-field data ($z_d = 5\lambda_0$) and near-field data measured at the distance $z_d = \lambda_0/2$.

The reconstructed objects are represented in 2D using a 40dB scale, whose reference is the maximum value of the plotted function. We also show the comparison between the original and reconstructed shapes in the plane $y = 0$ (1D plots).

3.4.2. Single monochromatic plane wave In the case of a single monochromatic incident plane wave, one has simply $u_i(\boldsymbol{r}) = \exp(i\boldsymbol{k}_i.\boldsymbol{r})$, where $\boldsymbol{k}_i$ is the incident wave vector with $|\boldsymbol{k}_i| = k$. As there is no noticeable change when the direction of incidence is modified, we only show here results for normal incidence, *i.e.*, for $\boldsymbol{k}_i = (0, 0, -k)$

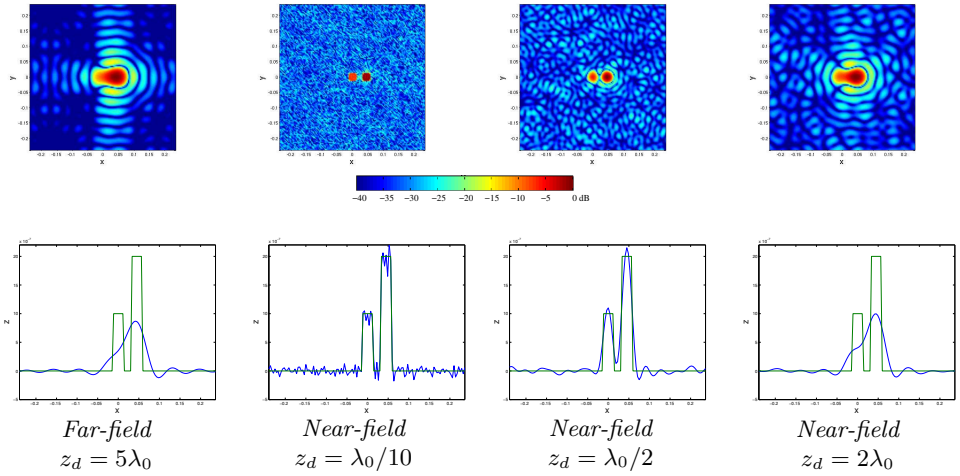

Figure 4. Single monochromatic plane wave, normal incidence. **SNR= 40 dB**. Reconstruction obtained with far-field data ($z_d = 5\lambda_0$) and with near-field data for $z_d = \lambda_0/10$, $z_d = \lambda_0/2$ and $z_d = 2\lambda_0$. Above: 40dB scale. Bottom: comparison between original and reconstructed shape in the plane $y = 0$.

For high signal-to-noise ratio (SNR = 40 dB), the reconstructions are represented on figure 4. As expected, since the two disks are too close, it is not possible to separate them using far-field data. On the other hand, the inversion using near-field data performs much better when measurements are made sufficiently close to the surface ($z_d = \lambda_0/10$ or $z_d = \lambda_0/2$). The improvement is spectacular when $z_d < \lambda_0$ while the result obtained with $z_d = 2\lambda_0$ is almost the same as the one obtained with far-field inversion. Notice also that the results obtained with near-field data are much

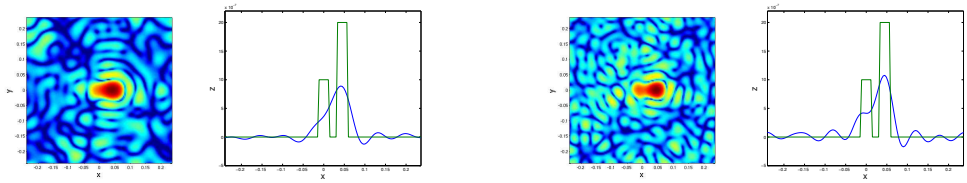

Far-field, $z_d = 5\lambda_0$ *Near-field,* $z_d = \lambda_0/2$

Figure 5. Single monochromatic plane wave, normal incidence. **SNR= 12 dB**. Reconstruction obtained with far-field data ($z_d = 5\lambda_0$) and with near-field data for $z_d = \lambda_0/2$. 40dB scale and comparison between original and reconstructed shape in the plane $y = 0$.

more corrupted by noise than the one obtained with far-field data. The amplification of the high spatial frequency components of the noise is clearly visible for $z_d = \lambda_0/10$, while it is smoother for $z_d = \lambda_0/2$. These results illustrate very well the trade-off between resolution and noise amplification.

Results obtained in the case of lower signal-to-noise ratio (SNR= 12 dB) are presented on figure 5. As expected, decrease in the SNR does not affect much the image obtained with the far-field data: the image is almost the same as the one obtained for the higher SNR, with a slightly higher speckle. This is one of the advantages of far field inversion: there is no noise amplification and thus the method is very robust to noise. On the other hand, when comparing the near-field image corresponding to $z_d = \lambda_0/2$ with the one obtained at higher SNR (see figure 4) we see that lower SNR clearly affects both the resolution and the noise level of the reconstructed image. This shows that near-field inversion is very sensitive to noise.

3.4.3. Beam of monochromatic plane waves We consider here the case of a beam of incident monochromatic plane waves, given by $u_i(\boldsymbol{r}) = \int_{\theta,\varphi} a(\theta,\varphi)\exp(ik\hat{\boldsymbol{k}}_i(\theta,\varphi).\boldsymbol{r})$, where $\hat{\boldsymbol{k}}_i(\theta,\varphi)$ is the unit vector defined in spherical coordinates associated to colatitude θ and longitude φ. $a(\theta,\varphi)$ is a normalized window function which defines the spread of the beam. In practice, it has a constant value around the central direction of incidence $\boldsymbol{k}_i^0$ with an opening angle of $\Delta\phi = 10°$ in both latitude and colatitude (see figure 6). The central direction of incidence is the normal incidence. We recall that the function obtained with the inversion process described in section §3 is $f(\boldsymbol{\rho}) = -h(x,y)\partial_z u_i(\boldsymbol{\rho},0)$. Thus, in order to recover the shape, h, one has to divide f by $\partial_z u_i(\boldsymbol{\rho},0)$. Since the beam of plane waves has a peak centered at the origin and then vanishes, we invert it only for the values which are above the cut-off of 5dB. This results in recovering the values of the shape $h(\boldsymbol{\rho})$ only in a disk centered at origin.

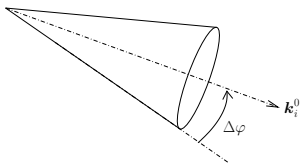

Figure 6. Description of the beam of monochromatic plane waves

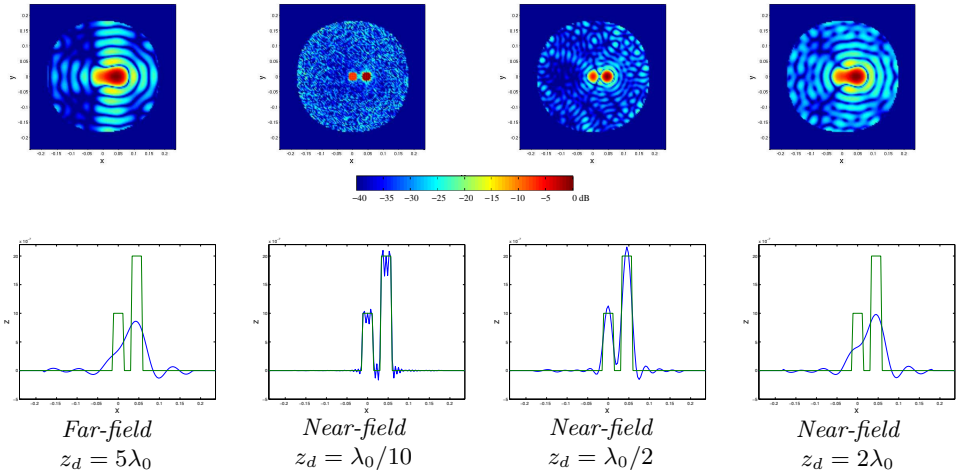

Figure 7. Beam of monochromatic plane waves, normal incidence. **SNR= 40 dB**. Reconstruction obtained with far-field data ($z_d = 5\lambda_0$) and with near-field data for $z_d = \lambda_0/10$, $z_d = \lambda_0/2$ and $z_d = 2\lambda_0$. Above: 40dB scale. Bottom: comparison between original and reconstructed shape in the plane $y = 0$.

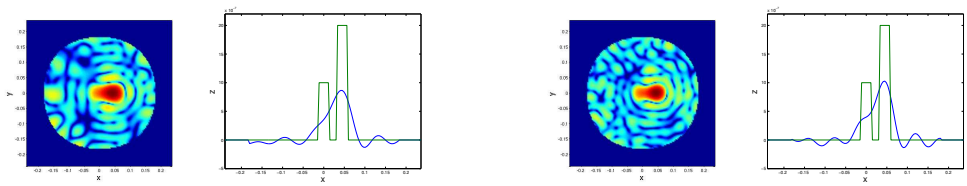

Figure 8. Beam of monochromatic plane waves, normal incidence. **SNR= 12 dB**. Reconstruction obtained with far-field data ($z_d = 5\lambda_0$) and with near-field data for $z_d = \lambda_0/2$. 40dB scale and comparison between original and reconstructed shape in the plane $y = 0$.

Results obtained with high SNR are represented on figure 7. They are very close to those obtained with a single monochromatic plane wave. The same holds for the results obtained with lower SNR presented on figure 8. Thus we can conclude that the use of a beam does not provide any improvement in the image reconstruction.

4. Use of a broadband incident plane wave

4.1. Broadband inversion method

If the incident wave is a plane wave with direction of incidence $\hat{\boldsymbol{k}}_i$, it can be written in the time domain $u_i(\boldsymbol{r}, t) = \psi(\frac{1}{c}\hat{\boldsymbol{k}}_i.\boldsymbol{r} - t)$, or equivalently, as a superposition of harmonic plane waves:

$$u_i(\boldsymbol{r}, t) = \frac{1}{(2\pi)} \int_\omega e^{i(\frac{\omega}{c}\hat{\boldsymbol{k}}_i.\boldsymbol{r} - \omega t)} \tilde{\psi}(\omega) d\omega,$$

where $\tilde{\psi}(\omega) = \int e^{-i\omega t}\psi(t)dt$ denotes the Fourier Transform with respect to the time variable of the function ψ.

For each pulsation ω in the bandwidth of $\tilde{\psi}$, it is possible to reconstruct an image of the displacement, using either far-field or near-field data. This image is denoted $f_\omega(\boldsymbol{\rho})$. Notice that ω plays here simply the role of a parameter and is not a variable. The broadband image is obtained by computing the average value of the family of images (f_ω), using the power spectrum of the function $\tilde{\psi}$ as weight, which leads to

$$f_{BB}(\boldsymbol{\rho}) = \frac{1}{\|\tilde{\psi}\|_2^2}\int_\omega f_\omega(\boldsymbol{\rho})|\tilde{\psi}(\omega)|^2 d\omega, \tag{23}$$

where $\|\tilde{\psi}\|_2$ denotes the L^2 norm of $\tilde{\psi}$. For a given angular frequency ω, we let $\hat{S}_{z_d}(\omega, \boldsymbol{\kappa})$ be the pseudo-inverse of the transfer function defined for either the far-field or near-field inversion and given by (13) or (17), respectively. Using (14) or (19), equation (23) can be written in the spatial Fourier domain as

$$\hat{f}_{BB}(\boldsymbol{\kappa}) = \hat{\mathcal{K}}_{BB}(\boldsymbol{\kappa})\hat{f}(\boldsymbol{\kappa}) + \hat{\mathcal{N}}_{BB}(\boldsymbol{\kappa}), \tag{24}$$

where

$$\begin{aligned} \hat{\mathcal{K}}_{BB}(\boldsymbol{\kappa}) &= \int \varphi(\omega)\mathbf{1}_{k_c(\omega)}d\omega, \\ \hat{\mathcal{N}}_{BB}(\boldsymbol{\kappa}) &= \int \varphi(\omega)\hat{S}_{z_d}(\omega, \boldsymbol{\kappa})\hat{n}(\omega, \boldsymbol{\kappa})d\omega. \end{aligned} \tag{25}$$

We have introduced here the weighting function $\varphi(\omega) = |\tilde{\psi}(\omega)|^2/\|\tilde{\psi}\|_2^2$. The cut-off spatial frequency $k_c(\omega)$ is given by $k_c(\omega) = \omega/c$ in the far-field case and by $k_c(\omega) = k_{NF}(\omega)$ in the near-field case, where k_{NF} is defined by (18). The first term of (24) provides a low pass filtered version of the function f while the second term is the resulting noise.

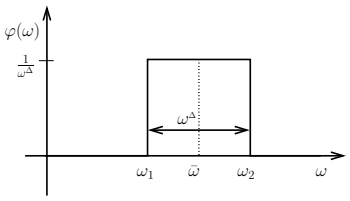

Figure 9. Step shaped power spectrum of the signal.

Results with SNR = 40dB are plotted in figure 10. In this example, $\varphi(\omega)$ is the simple step shaped function shown in figure 9, that is, $\varphi(\omega) = 1/(\omega_2 - \omega_1)$ for $\omega \in [\omega_1, \omega_2]$ and 0 elsewhere. The central angular frequency is defined by $\bar{\omega} = (w_1 + w_1)/2$ and the angular bandwidth by $\omega^\Delta = w_2 - w_1$. The central frequency used in the experiments is 5 GHz and the frequency range is from 2.5 GHz to 7.5 GHz, which corresponds to 100% relative bandwidth. All other parameters are the same as those used in section §3.4. A small improvement of the resolution in comparison to the narrowband case is clearly visible in the figures. However it remains difficult to distinguish the two circles in the far-field case even with a very large bandwidth. The analysis of the kernel $\mathcal{K}_{BB}$ associated to the reconstruction of these images and defined by (25) allows for characterizing the improvement of the resolution. This analysis is presented in the next section.

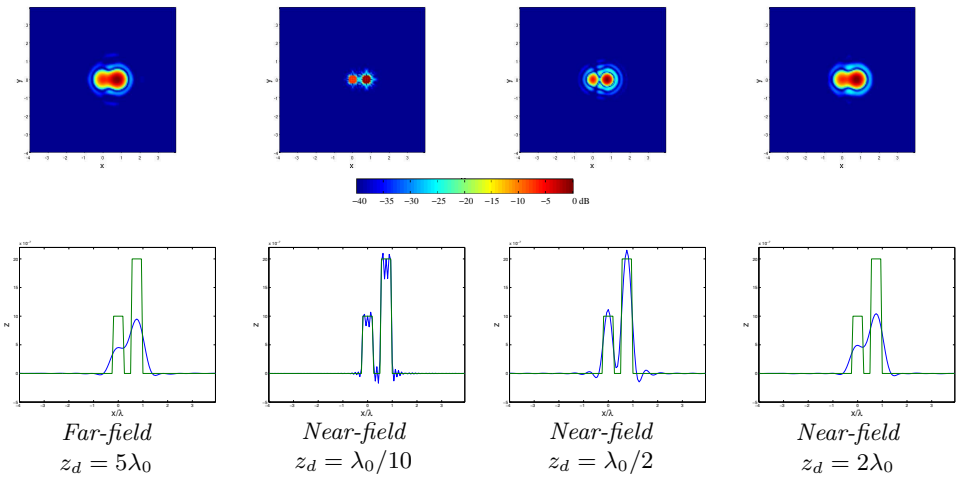

Far-field $z_d = 5\lambda_0$ | *Near-field* $z_d = \lambda_0/10$ | *Near-field* $z_d = \lambda_0/2$ | *Near-field* $z_d = 2\lambda_0$

Figure 10. Broadband plane wave (central frequency 5 GHz, bandwidth = 100%), normal incidence. **SNR= 40 dB**. Reconstruction obtained with far-field data ($z_d = 5\lambda_0$) and with near-field data for $z_d = \lambda_0/10$, $z_d = \lambda_0/2$ and $z_d = 2\lambda_0$. Above: 40dB scale. Bottom: comparison between original and reconstructed shape in the plane $y = 0$.

In addition, the integration over the bandwidth results in a clearly visible reduction of speckles. This is a consequence of the fact that the additive noise $n(t, \boldsymbol{\rho})$ is assumed to be stationary and uncorrelated in both time and space and thus uncorrelated in both angular frequencies and spatial frequencies. For a stationary and uncorrelated random process $X(\omega)$ with mean zero and variance σ^2, that is, such that

$$\langle X(\omega)\rangle = 0 \quad \text{and} \quad \langle X(\omega)\bar{X}(\omega')\rangle = \sigma^2\delta(\omega - \omega'),$$

the integral $N = \int \varphi(\omega)X(\omega)d\omega$ is a random variable which satisfies

$$\langle N\rangle = 0 \quad \text{and} \quad \langle N^2\rangle = \sigma^2 \int \varphi(\omega)^2 d\omega.$$

For the weight φ given above the variance of N is $\langle N^2\rangle = \sigma^2/(w_2 - w_1)$ and thus the larger the bandwidth, the lower the level of the averaged noise. Similarly, an estimate of the level of the noise $\mathcal{N}_{BB}(\boldsymbol{\rho})$ can be given by computing its covariance.

The main effect of broadband inversion with far-field data is to decrease the noise level. For inversion with near-field data, however, since the resolution is limited by the SNR, it is possible to take advantage of the noise reduction in order to improve the resolution. This means that we can use a higher value for the cut-off spatial frequency $k_c(\omega)$ in (25) without degrading the reconstructed image, as would be the case with narrowband inversion.

This idea is illustrated in figures 11 and 12 which show the results obtained for near-field inversion with SNR = 12dB and $z_d = \lambda_0/2$ in the narrowband case and in the broadband case with 100% bandwidth. Figure 11 is obtained with $k_c(\omega) = k_{NF}(\omega)$ given by (18) while figure 12 is obtained with $k_c(\omega) = 1.9k_{NF}(\omega)$, that is 90% higher. First, in the narrowband case, the use of a higher value of the threshold $k_c(\omega)$ produces a very noisy image in which the object is completely lost. However, in the broadband case, since the noise is averaged the use of a higher cut-off frequency produces an image

with better resolution and without a lot of noise. The two disks are now well separated, which was not the case with narrowband inversion or with broadband inversion with a lower value of $k_c(\omega)$. This result shows clearly the significance of using broadband signals in near-field imaging. Of course, there is a limiting cut-off for the broadband case also, after which the image will be very corrupted by noise. This cut-off is in general higher than the one obtained in the narrowband case and that is why we expect an improvement in resolution. We will describe two methods for choosing the cut-off in the broadband case in section §4.3.

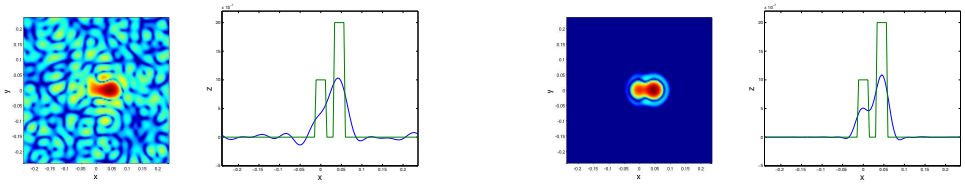

Narrowband *100% bandwidth*

Figure 11. Reconstructions obtained with near-field data for normal incidence illumination and measurements at $z_d = \lambda_0/2$. SNR= 12 dB. **The cut-off frequency is $k_c(\omega) = k_{NF}(\omega)$.** Left narrowband inversion and right broadband inversion (Central frequency 5 GHz, bandwidth = 100%). 40dB scale and comparison between original and reconstructed shape in the plane $y = 0$.

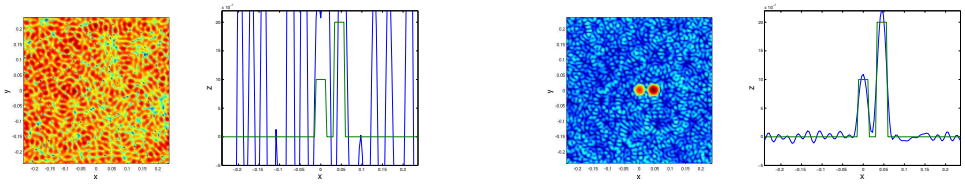

Narrowband *100% bandwidth*

Figure 12. Reconstructions obtained with near-field data for normal incidence illumination and measurements at $z_d = \lambda_0/2$. SNR= 12 dB. **The cut-off frequency is $k_c(\omega) = 1.9k_{NF}(\omega)$.** Left narrowband inversion and right broadband inversion (Central frequency 5 GHz, bandwidth = 100%). 40dB scale and comparison between original and reconstructed shape in the plane $y = 0$.

4.2. Resolution analysis of the broadband inversion

In this section we give the analysis of the kernel $\mathcal{K}_{BB}$ associated to the broadband inversion method discussed above. The analysis is performed in the 2D case (and thus for a 1D boundary), which simplify the computations.

Far-field broadband inversion The Fourier Transform of the far-field broadband kernel $\hat{\mathcal{K}}^{FF}_{BB}(\kappa)$ introduced in (25) is given by:

$$\hat{\mathcal{K}}^{FF}_{BB}(\kappa) = \int \varphi(\omega)\mathbf{1}_{\frac{\omega}{c}}(\kappa)d\omega = \int_{\omega \geq c|\kappa|}^{\infty} \varphi(\omega)d\omega, \quad \forall \kappa \in \mathbb{R}. \tag{26}$$

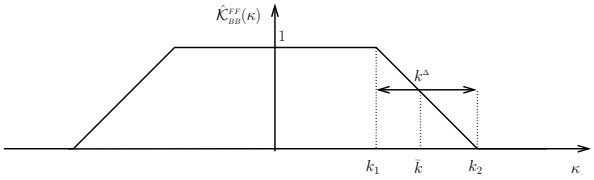

Figure 13. The Fourier Transform of the far-field broadband kernel $\hat{\mathcal{K}}^{FF}_{BB}(\kappa)$ in the 2D case for a step-shaped φ.

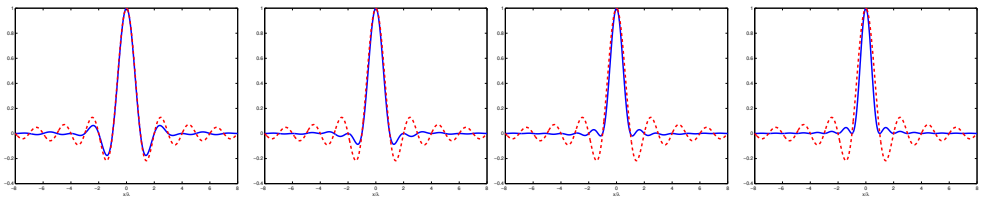

Figure 14. The Imaging Point Spread Function **for a 1D boundary** in the broadband case for different values of bandwidth (—) compared to the kernel in the narrowband case at central frequency (- - -) [all curves are normalized so that $\mathcal{K}^{FF}_{NB}(0) = 1$]

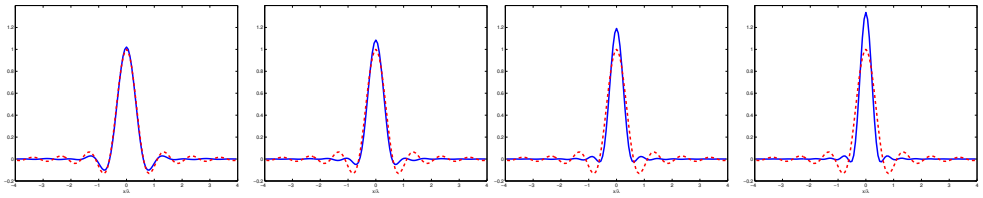

Figure 15. The Imaging Point Spread Function **for a 2D boundary** in the broadband case for different values of bandwidth (—) compared to the kernel in the narrowband case at central frequency (- - -) [all curves are normalized so that $\mathcal{K}^{FF}_{NB}(0) = 1$]

It is shown in figure 13. It can be written as a convolution

$$\hat{\mathcal{K}}^{FF}_{BB}(\kappa) = \frac{1}{k^\Delta}\mathbf{1}_{\bar{k}} \star \mathbf{1}_{k^\Delta/2}(\kappa), \quad \forall \kappa \in \mathbb{R}. \tag{27}$$

where we introduced the central wave number $\bar{k} = \bar{\omega}/c$ and $k^\Delta = \omega^\Delta/c$, with ω^Δ the angular frequency bandwidth. In the space domain the kernel is therefore given by

$$\mathcal{K}^{FF}_{BB}(x) = \frac{\bar{k}}{\pi}\mathrm{sinc}(\bar{k}x)\mathrm{sinc}(\frac{k^\Delta x}{2}). \tag{28}$$

We recall that in the narrowband case, at the central frequency and for a 1D boundary, the kernel is the inverse Fourier Transform of the characteristic function $\mathbf{1}_{\bar{k}}$, that is

$$\mathcal{K}^{FF}_{NB}(x) = \frac{\bar{k}}{\pi}\mathrm{sinc}(\bar{k}x). \tag{29}$$

The kernels for different values of the bandwidth are shown in figure 14 for a central frequency of 5GHz. We see that the effects of integrating over the bandwidth are (i) a decrease in the size of the side lobes of the kernel compared to the narrowband case and (ii) a decrease in the width of the central peak when the bandwidth is larger than 100% (*i.e.*, for $k^{\Delta} \geq \bar{k}$). When the width of the central peak is the same for narrowband and broadband data, we still see a slight improvement in the resolution (compare Figure 10 with Figure 4). This suggests that the Rayleigh criterion used in section §3 to define the resolution is rather crude as it does not take into account the level of the side lobes. Many other criteria have been proposed in order to provide a more realistic measure of resolution, but it is not our purpose here to address this question in detail (see for example [13]).

4.3. Selection of the cut-off $k_c(\omega)$ in the case of broadband inversion

In order to determine the cut-off $k_c(\omega)$ in the case of broadband near-field inversion we analyze in this section the amplification of the back-propagated noise $\hat{\mathcal{N}}_{BB}(\kappa)$. The difference between the estimate $\hat{f}_\omega(\kappa)$ and the true surface displacement $\hat{f}(\kappa)$ is,

$$\hat{e}(\omega,\kappa) = \begin{cases} \hat{S}^{-}_{z_d}(\omega,\kappa)\hat{n}(\omega,\kappa) & \text{for } |\kappa| \geq k_c(\omega) \\ -\hat{f}(\kappa) & \text{else.} \end{cases} \tag{30}$$

After integration over the bandwidth B and a small interval of wavenumbers Δ we obtain

$$\begin{aligned} \lim_{\Delta\to 0} \frac{1}{\Delta} E\{ \int_{\Delta}\int_{B} |\hat{e}(\omega,\kappa)|^2 d\omega d\kappa\} \\ \leq \int_{B} \mathbf{1}_{\{|\kappa|\leq k_c(\omega)\}} |\hat{S}_{z_d}(\omega,z_d)|^{-2} \varphi(\omega)^2 N^2 d\omega \end{aligned} \tag{31}$$

where $N^2 = \max_{\kappa,\omega} \hat{R}_{nn}(\omega,\kappa)$ is an estimation of the noise level.

In the following, we consider again the function $\varphi(\omega)$ shown in Figure 9. We have that $\varphi^2(\omega) = 1/\Delta B \varphi(\omega)$. As in the narrowband case, we require that this variance be smaller than the power of the signal P^2. In other words, we require that

$$\mathcal{F}(\kappa) = \int_{\omega_1}^{\omega_2} \mathbf{1}_{\{|\kappa|\leq k_c(\omega)\}} |\hat{S}_{z_d}(\omega,z_d)|^{-2} d\omega \leq \Delta B (\mathrm{SNR})^2. \tag{32}$$

We introduce the following dimensionless variables:

$\omega' = \omega/\bar{\omega}$	the relative angular frequency
$\beta = B/\bar{\omega}$	the relative bandwidth
$\bar{k} = \bar{\omega}/c$	the central wavenumber
$\kappa' = \lvert\kappa\rvert/\bar{k}$	the relative wavenumber
$k'_c(\omega) = k_c(\omega)/\bar{k}$	the relative cut-off wavenumber
$\alpha = z_d\bar{k}$	the dimensionless distance of measurements.

Equation (32) can then be written as

$$\mathcal{F}'(\kappa') = \frac{1}{\beta} \int_{1-\beta/2}^{1+\beta/2} \mathbf{1}_{\{\kappa'\leq k'_c(\omega')\}}(\kappa') e^{-2i\alpha\sqrt{\omega'^2-\kappa'^2}} d\omega' \leq (\beta\bar{\omega})(\mathrm{SNR})^2 \tag{33}$$

and we have $\mathcal{F}(\kappa) = \mathcal{F}'(|\kappa|/\bar{k})$. We shall now consider two different ways of choosing the cut-off $k'_c(\omega')$.

4.3.1. Uniform cut-off. We first consider the case of a uniform cut-off, independent of the frequency ω. It is defined by

$$k_c^{opt} = \max\{\kappa' \ / \ \mathcal{F}'_\infty(\kappa') \leq (\beta\bar{\omega})(\mathrm{SNR})^2\}. \tag{34}$$

Here $\mathcal{F}'_\infty$ is the function $\mathcal{F}'$ obtained when no cut-off is used, that is, for $k'_c(\omega') = \infty$.

The computation of $\mathcal{F}'_\infty(\kappa')$ and the resolution of (34) are done numerically. The cut-off values k_c^{opt} obtained using (34) for different signal to noise ratios and distances of observation are given in table 2. Here the central frequency is 5GHz and the relative bandwidth is 100%. We note that k_c^{opt} is the relative cut-off wavenumber which is equal to the ratio R_{FF}/R_{NF} so that we can compare table 2 with table 1. There is considerable improvement compared to the narrowband case. However, when the SNR is very low and the distance of measurements is relatively big, equation (34) leads to a cut-off wavenumber that is smaller than some of the wavenumbers in the available bandwidth. This is what happens for example in table 2 for $z_d/\lambda_0 = 2$ and $\mathrm{SNR} = 20dB$ or $12dB$. In this case the images $\hat{f}_{\omega'}$ constructed at frequencies $\omega' \geq k_c^{opt}$ are less resolved than the far-field estimates. This is because we use a uniform value for the cut-off and by trying to control the amplification of the noise at low frequencies we penalize the higher frequencies. In such cases another strategy should be followed. We propose such a strategy in the next section.

	Distance of observation z_d/λ_0				
SNR	1/10	1/5	1/2	1	2
40 dB	26.5840	13.3220	5.4051	2.7998	1.5074
20 dB	22.9226	11.4959	4.6852	2.4487	1.3403
12 dB	21.4658	10.7699	4.3999	2.3100	1.2750

Table 2. Improvement of the resolution for **broadband** near-field inversion: values of k_c^{opt} for different values of noise and observation distance. The central frequency is 5GHz and the relative bandwidth is 100%

For a constant cut-off wavenumber the global transfer function is

$$\hat{\mathcal{K}}_{BB}(\kappa) = \frac{1}{\beta}\int_{1-\beta/2}^{1+\beta/2} \mathbf{1}_{\{|\kappa|/\bar{k} \leq k_c^{opt}\}} d\omega' = \mathbf{1}_{\{|\kappa|/\bar{k} \leq k_c^{opt}\}}, \tag{35}$$

and thus the global point spread function (PSF) is a Bessel function (as for the narrowband case) whose central peak's width is $1.22\pi/(\bar{k}k_c^{opt})$. Contrary to what occurs in the far-field broadband inversion, there is no attenuation of the side lobes in this case. There is, however, a significant improvement in resolution as the central peak is now much narrower than in the narrowband case.

4.3.2. Proportional cut-off. We consider now a cut-off wavenumber which is proportional to the one used in the narrowband case. That is, we take

$$k'_c(\omega') = \gamma k'_{NF}(\omega'),$$

with $k'_{NF}(\omega')$ defined by (18), which is recast in dimensionless variables

$$k'_{NF}(\omega') = \sqrt{\omega'^2 + (\log \mathrm{SNR}/(\alpha))^2}.$$

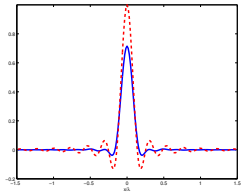

Figure 16. The Imaging Point Spread Function **for a 2D boundary** for near-field broadband inversion with a frequency dependent cut-off $k_c'(\omega) = \gamma^{opt} k_{NF}'(\omega')$ (—) and with a uniform one $k_c'(\omega') = k_c^{opt}$ (- - -). $z_d = .5\lambda_0$, SNR $= 12dB$. The central frequency is 5GHz and the relative bandwidth is 100 %. [the curves are normalized so that $\mathcal{K}_{k_c^{opt}}(0) = 1$]

We denote by $\mathcal{F}_\gamma'$ the corresponding function defined by (33) and note that the family $(\mathcal{F}_\gamma')_\gamma$ is increasing with respect to the parameter γ. The optimal value of the proportionality constant γ is given by the constraint (33), which reduces to

$$\gamma^{opt} = \max\{\gamma \text{ s.t. } \mathcal{F}_\gamma' \leq \beta(\text{SNR})^2\} \tag{36}$$

In the case where the SNR $= 12dB$ and $z_d/\lambda_0 = 1/2$ at central frequency 5GHz, and with a relative bandwidth of 100%, we obtain $\gamma_{opt} = 3.26$ so that the cut-offs at the lowest and highest frequencies are $k_c'(\omega_1') = 2.17$ and $k_c'(\omega_2') = 5.1$ respectively. Not surprisingly, the value of k_c^{opt} $(= 4.3999)$ obtained in Table 2 is between these extremes. This strategy allows for cutting-off at higher spatial frequency in the higher range of the bandwidth while using a smaller cut-off in the lower range of the bandwidth. In this case, it is not possible to compute analytically the global point spread function. A numerical approximation is shown in Figure 16 and is compared to the one obtained with uniform cut-off. We note that with the proportional cut-off we do have an attenuation of the side lobes.

4.4. Numerical results: A comparison between the different cut-off wavenumbers

We consider here the same setup as in section §3.4. The central frequency used in the experiments is 5 GHz and the frequency range is from 2.5 GHz to 7.5 GHz corresponding to 100% relative bandwidth.

We compare the following different choices of cut-off wavenumbers for measurements made at distance $z_d = \lambda_0/2$ and SNR $= 12dB$:

- $k_c(\omega) = 3.26 k_{NF}(\omega)$, *i.e.* , $\gamma = \gamma^{opt}$ as determined in the section §4.3.2, the results are shown in Figure 17,
- $k_c(\omega) = 4.39\bar{k}$ *i.e.* a uniform cut-off with the optimal value computed in section §4.3.1, the results are shown in Figure 18,
- and $k_c(\omega) = 5.2\bar{k}$ *i.e.* a uniform cut-off with higher value than the optimal one for which the results displayed in Figure 19.

These results should also be compared with the ones of figures 11 and 12 where non-optimal values for γ are used, that is $k_c(\omega) = k_{NF}(\omega)$, $\gamma = 1$ for Figure 11 and $k_c(\omega) = 1.9 k_{NF}(\omega)$, $\gamma = 1.9$ for Figure 12.

We see in figures 17 and 18 that the results obtained by both methods for the optimal cut-off values are very good and we can distinguish clearly the two objects.

These results are much better than the one obtained with the naive use of $\gamma = 1$ (see Figure 11).

As in the narrowband case there is a trade-off between resolution and noise amplification that is illustrated by the results in Figure 19 where a higher value than the optimal cut-off is used. In this case one obtains a much worse image.

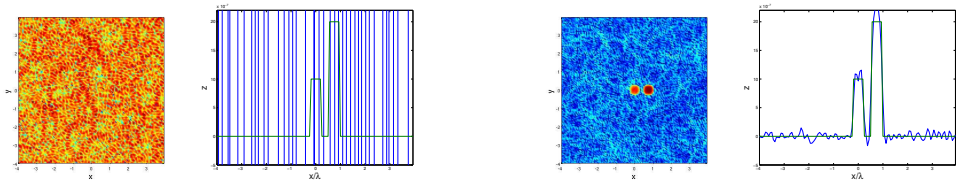

Narrowband *100% bandwidth*

Figure 17. Reconstruction of the shape obtained with near-field data for normal incidence illumination and measurements at $z_d = \lambda_0/2$. SNR= 6 dB. **The cut-off frequency is $k_c(\omega) = 3.26 k_{NF}(\omega)$.** Left narrowband inversion and right broadband inversion (Central frequency 5 GHz, bandwidth = 100%). 40dB scale and comparison between original and reconstructed shape in the plane $y = 0$.

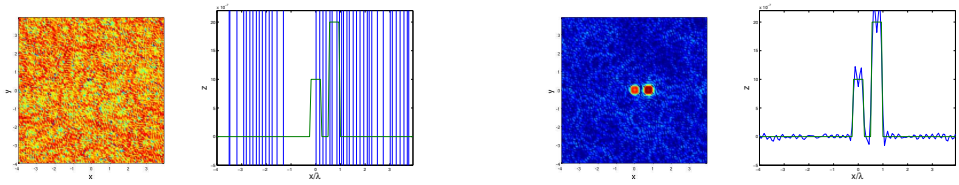

Narrowband *100% bandwidth*

Figure 18. Reconstruction of the shape obtained with near-field data for normal incidence illumination and measurements at $z_d = \lambda_0/2$. SNR= 6 dB. **The cut-off frequency is uniform $k_c(\omega) = 4.39\bar{k} = k_c^{opt}\bar{k}$.** Left narrowband inversion and right broadband inversion (Central frequency 5 GHz, bandwidth = 100%). 40dB scale and comparison between original and reconstructed shape in the plane $y = 0$.

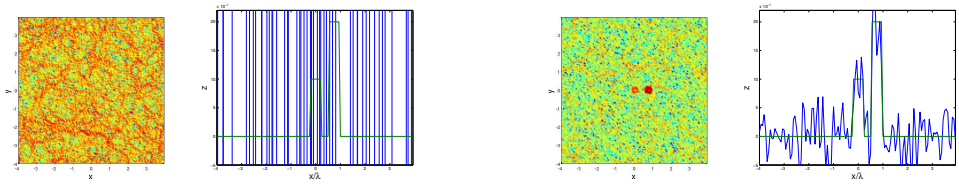

Narrowband *100% bandwidth*

Figure 19. Reconstruction of the shape obtained with near-field data for normal incidence illumination and measurements at $z_d = \lambda_0/2$. SNR= 6 dB. **The cut-off frequency is uniform $k_c(\omega) = 5.2\bar{k}$.** Left narrowband inversion and right broadband inversion (Central frequency 5 GHz, bandwidth = 100%). 40dB scale and comparison between original and reconstructed shape in the plane $y = 0$.

5. Summary and Conclusions

In the first part of the paper we have reviewed near and far-field imaging of small surface displacements in the narrowband regime. We considered carefully the trade-off between distance of the measurements from the surface and the signal to noise ratio, which determines the frequency cut-off that regularizes the inversion. We have illustrated the theory with numerical simulations.

The main results of the paper are in the second part, which is an analysis of the extension of near-field imaging to broadband regimes. We have found that inversions with broadband signals have better resolution at a given noise level because of frequency averaging. The suppression of speckles in broadband images effectively increases the SNR, which determines the frequency cut-off in the regularization of the inversion. This is the reason why smaller scale evanescent waves can be used in the inversion, which gives better image resolution. We have illustrated the theory with the results of several numerical simulations.

is independent of the discretization.

Acknowledgments

The work of G. Derveaux, G. Papanicolaou and C. Tsogka was partially supported by the Office of Naval Research N00014-02-1-0088, by the National Science Foundation DMS-0354674-001 and by DARPA/ARO 02-SC-ARO-1067-MOD 1.

References

[1] G. S. Agarwal, *Subwavelength resolution using evanescent waves*, Pure Appl. Opt., 7 (1998), pp. 1143–1149.

[2] M. Bertero, P. Boccacci, and M. Piana, *Resolution and super-resolution in inverse diffraction*, in Inverse problems of wave propagation and diffraction (Aix-les-Bains, 1996), vol. 486 of Lecture Notes in Phys., Springer, Berlin, 1997, pp. 1–17.

[3] M. Bertero and P. Boccaci, *Introduction to inverse problems in imaging*, Institute of Physics Publishing, Bristol, 1998.

[4] L. Borcea, G. Papanicolaou, and C. Tsogka, *Theory and applications of time reversal and interferometric imaging*, Inverse Problems, 19 (2003), pp. 5139–5164.

[5] L. Borcea, G. Papanicolaou, and C. Tsogka, *Adaptive interferometric imaging in clutter*. Preprint, 2005.

[6] ———, *Coherent interferometry in finely layered random media*. to appear SIAM J. on Mult. Model. and Simul., 2005.

[7] G. V. Borgiotti, A. Sarkissian, E. G. Williams, and L. Schuetz, *Conformal generalized near-field acoustic holography for axisymmetric geometries*, J. Acoust. Soc. Am., 88 (1990), pp. 199–209.

[8] M. Born and E. Wolf, *Principles of Optics*, Academic Press, New York, 1970.

[9] A. S. Carasso, *Linear and nonlinear image deblurring:a documented study*, SIAM J. Numer. Anal., 36 (1999), pp. 1659–1689.

[10] P. Carney and J. Schotland, *Inverse scattering for near-field microscopy*, Applied Physics Letters, 77 (2000), pp. 2798–2800.

[11] D. Courjon and C. Bainier, *Near field microscopy and near field optics*, Rep. Prog. Phys., 57 (1994), pp. 989–1028.

[12] C. Girard and A. Dereux, *Near-field optics theories*, Rep. Prog. Phys., 59 (1996), pp. 657–699.

[13] A. W. Jones, J. Bland-Hawthorn, and S. P. L., *Towards a general definition for spectroscopic resolution*, in Astronomical Data Analysis Software and Systems IV, ASP Conferences Series, 1995. R. A. Shaw, H. E. Paye and J. J. E. Hayes, eds.

[14] E. Lalor, *Conditions for validity of the angular spectrum of plane waves*, J. Opt. Soc. Am., 58 (1968), pp. 1235–1237.

[15] K. Miller, *Least squares methods for ill-posed problems with a prescribed bound*, SIAM J. Math. Anal., 1 (1970), pp. 52–74.
[16] G. S. Smith and L. E. Rickard Petersson, *On the use of evanescent electromagnetic waves in the detection and identification of objects buried in lossy soil*, IEEE Transactions on Antennas and Propagation, 48 (2000), pp. 1295–1300.
[17] A. Sommerfeld, *Optics*, Academic Press, New York, 1964.
[18] E. G. Williams and H. D. Dardy, *Nearfield acoustical holography using an underwater, automated scanner*, J. Acoust. Soc. Am., 78 (1985), pp. 789–798.
[19] E. G. Williams, H. D. Dardy, and K. B. Washburn, *Generalized nearfield acoustical holography for cylindrical geometry: Theory and experiment*, J. Acoust. Soc. Am., 81 (1987), pp. 389–407.
[20] E. G. Williams, B. H. Houston, and J. A. Bucaro, *Broadband near-field acoustical holography for vibrating cylinders*, J. Acoust. Soc. Am., 86 (1989), pp. 674–679.
[21] E. G. Williams, J. Maynard, and E. Skudrzyk, *Sound source reconstructions using a microphone array.*, J. Acoust. Soc. Am., 68 (1980), pp. 340–344.
[22] E. G. Williams and J. D. Maynard, *Holographic imaging without the wavelength resolution limit.*, Phys. Rev. Letters., 45 (1980), pp. 554–557.
[23] E. G. Williams, J. D. Maynard, and Y. Lee., *Near-field acoustic holography:i. theory of generalized holography and the development of nah*, J. Acoust. Soc. Am., 78 (1985), pp. 1395–1413.